



HAL
open science

Photocatalytic dihydroxylation of light olefins to glycols by water.

Chunyang Dong, Yinghao Wang, Z. Deng, W. Wang, Maya Marinova, Karima Ben Tayeb Meziane, Jean-Charles Morin, Mélanie Dubois, Martine Trentesaux, Yury Kolyagin, et al.

► **To cite this version:**

Chunyang Dong, Yinghao Wang, Z. Deng, W. Wang, Maya Marinova, et al.. Photocatalytic dihydroxylation of light olefins to glycols by water.. Nature Communications, 2024, Nature Communications, 15, pp.8210. 10.1038/s41467-024-52461-9 . hal-04773090

HAL Id: hal-04773090

<https://hal.univ-lille.fr/hal-04773090v1>

Submitted on 8 Nov 2024

HAL is a multi-disciplinary open access archive for the deposit and dissemination of scientific research documents, whether they are published or not. The documents may come from teaching and research institutions in France or abroad, or from public or private research centers.

L'archive ouverte pluridisciplinaire **HAL**, est destinée au dépôt et à la diffusion de documents scientifiques de niveau recherche, publiés ou non, émanant des établissements d'enseignement et de recherche français ou étrangers, des laboratoires publics ou privés.



Distributed under a Creative Commons Attribution - NonCommercial - NoDerivatives 4.0 International License

Photocatalytic dihydroxylation of light olefins to glycols by water

Received: 23 February 2024

Accepted: 10 September 2024

Published online: 18 September 2024

Check for updates

Chunyang Dong^{1,2,9}, Yinghao Wang^{1,9}, Ziqi Deng^{2,9}, Wenchao Wang³, Maya Marinova⁴, Karima Ben Tayeb⁵, Jean-Charles Morin¹, Melanie Dubois¹, Martine Trentesaux¹, Yury G. Kolyagin¹, My Nghe Tran¹, Vlad Martin-Diaconescu⁶, Olga Safonova⁷, Jeremie Zaffran⁸, Andrei Y. Khodakov¹✉ & Vitaly V. Ordonsky¹✉

Aliphatic diols such as ethylene and propylene glycol are the key products in the chemical industry for manufacturing polymers. The synthesis of these molecules usually implies sequential processes, including epoxidation of olefins using hydrogen peroxide or oxygen with subsequent hydrolysis to glycols. Direct hydroxylation of olefins by cheap and green oxidants is an economically attractive and environmentally friendly route for the synthesis of diols. Here, we report a photocatalytic reaction for the dihydroxylation of ethylene and propylene to their glycols at room temperature using water as the oxidant. The photocatalyst contains Pd clusters stabilized by sub-nanometric polyoxometalate with TiO₂ as the host material. Under light irradiation, it results in production rates of ethylene glycol and propylene glycols of 146.8 mmol·g_{Pd}⁻¹·h⁻¹ and 28.6 mmol·g_{Pd}⁻¹·h⁻¹ with liquid-phase selectivities of 63.3 % and 80.0 %, respectively. Meanwhile, green hydrogen derived from water is produced as another valuable product. Combined spectroscopy investigation suggests that the reaction proceeds via π-bonded adsorption of olefins over Pd clusters with hydroxylation by hydroxyl radicals formed by photocatalytic dissociation of water.

Vicinal diols or glycols of light olefins are essential industrial compounds widely used in manufacturing polyesters, antifreeze, pharmaceuticals and other important products. The large-scale production of ethylene and propylene glycols (EG and PG) reaches about 60 million metric tons annually. The main route for the production of these compounds includes two steps, with the first oxidation of ethylene and propylene by oxygen or H₂O₂, respectively, to their epoxides, with subsequent acidic hydrolysis to diols (Fig. 1a)^{1–4}. Despite the high

productivity, such processes suffer from safety risk, high energy consumption and low selectivity, therefore, the one-step synthesis of diols by hydroxylation of olefins under mild reaction conditions would be highly desirable.

The direct route for the oxidation of alkenes to diols by osmium tetroxide was proposed by Hoffmann in 1912. The reaction proceeds by cycloaddition of OsO₄ to double bond with the formation of intermediate osmate ester further hydrolyzing to

¹UCCS–Unité de Catalyse et Chimie du Solide, Université de Lille, CNRS, Centrale Lille, ENSCL, Université d’Artois, UMR, 8181 Lille, France. ²Department of Chemistry, The University of Hong Kong, Hong Kong, China. ³School of New Energy, Nanjing University of Science & Technology, Jiangyin 214443, China. ⁴UMET–Institut Michel-Eugène Chevreul, Université de Lille, CNRS, INRAE, Centrale Lille, Université d’Artois, FR, 2638 Lille, France. ⁵Université de Lille, CNRS, UMR 8516 - LASIRE - Laboratoire de Spectroscopie pour les Interactions, la Réactivité et l’Environnement, F-, 59000 Lille, France. ⁶ALBA Synchrotron – CELLS, Carrer de la Llum 2-26, 08290 Cerdanyola del Vallès Barcelona, Spain. ⁷Paul Scherrer Institute, 5232 Villigen, Switzerland. ⁸Eco-Efficient Products and Processes Laboratory (E2P2L), UMI 3464 CNRS-Solvay, Shanghai, China. ⁹These authors contributed equally: Chunyang Dong, Yinghao Wang.

✉ e-mail: Andrei.Khodakov@univ-lille.fr; Vitaly.Ordonsky@univ-lille.fr

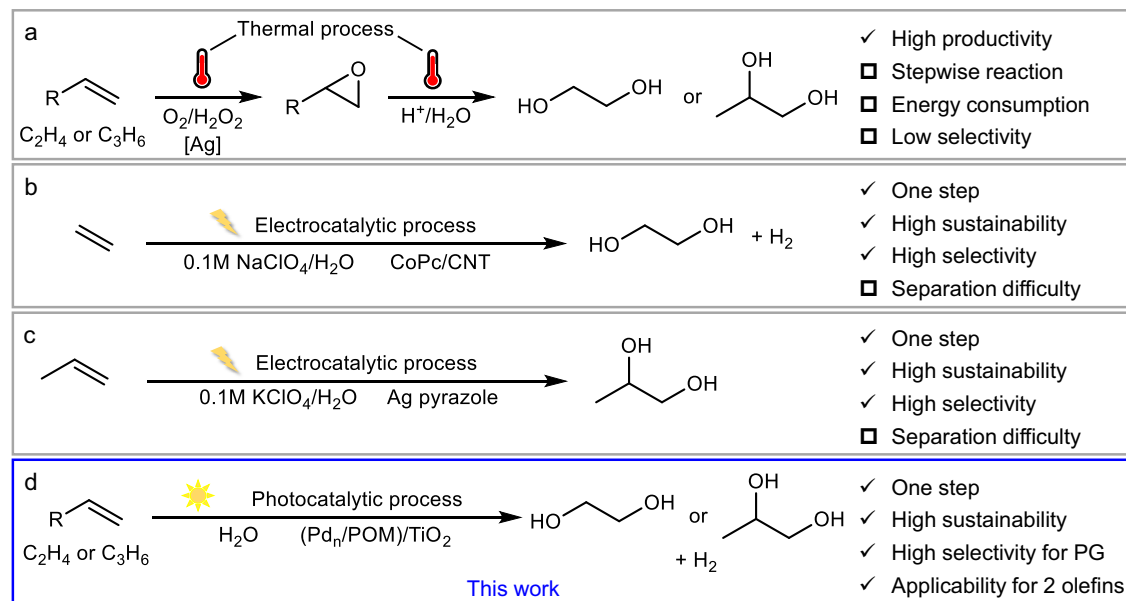
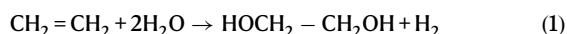


Fig. 1 | Schematic of different processes. a–d Illustration of different reaction processes to synthesize glycols from olefins, and their main advantages and disadvantages comparisons. Note that the CoPC/CNT in (a), POM and PG in (d) means

carbon nanotube supported cobalt phthalocyanine catalyst, polyoxometalate and propylene glycol, respectively.

vicinal diol⁵. The reaction is stoichiometric and requires the addition of terminal oxidants such as N-methylmorpholine N-oxide or $\text{K}_3\text{Fe}(\text{CN})_6$ for the catalytic route. Although the process is very selective and is used in the pharmaceutical industry for the production of bioactive diols, the high toxicity and high cost of OsO_4 and its terminal oxidants prompt researchers to look for alternative routes.

In recent years, to overcome the aforementioned problems of thermal processes, alternative catalytic systems for the synthesis of light glycols with both economic and environmental significance have been developed^{16–15}. With ethylene or propylene as starting reagents, the direct synthesis of EG or PG is currently achieved by electrocatalytic processes (e.g., Fig. 1b, c). For instance, by using pre-synthesized H_2O_2 as an oxidant, Wang demonstrated a cascade process to transform ethylene to ethylene oxide and followed with acidic hydrolysis to EG¹¹. Recently, Duan et al. established an efficient one-step transformation of ethylene to EG, using H_2O as an oxidant and a carbon nanotube stabilized molecular Co-phthalocyanine as a catalyst¹⁵. Moreover, Geng developed a molecular Ag pyrazole catalyst with reversible protonation properties, exhibiting remarkable performance in catalyzing propylene and H_2O into PG¹². Yet, the utilization of liquid electrolytes and/or stepwise operations among the current electrocatalytic processes will add, inevitably, extra cost for the products' synthesis and separation¹⁶. Thus, mild and selective catalytic dihydroxylation of olefins to the corresponding glycols using pure water as an oxidant would be highly desirable. In this case, except for the production of glycols, hydrogen as another valuable product was also obtained. However, unfavorable thermodynamics restricts this type of reaction in thermocatalysis (Eqs. 1–2 and Supplementary Fig. 1).



Photocatalysis provides an opportunity to overcome thermodynamic limitations by the separation oxidation and reduction stages

using photoexcited charge carriers (electrons and holes)^{17–27}. Recently, we realized a direct photocatalytic reaction route to the synthesis of acetic acid from CH_4 , CO and H_2O under mild conditions²³. Without light irradiation, such a process can hardly take place due to unfavorable thermodynamics. Herein, we report a photocatalytic reaction route for the direct dihydroxylation of ethylene and propylene into their glycols at ambient temperature, using H_2O as the oxygen source (Fig. 1d). The catalyst consists of Pd clusters stabilized by polyoxometalate clusters, with TiO_2 serving as the host semiconductor, in contrast to the single Pt atoms used in the previous work²³. The strong interaction between the acidic heteropolyacid unit and the Pd clusters on the TiO_2 surface facilitates efficient electron transfer to the metal sites. Simultaneously, the oxidation of water to hydroxyl radicals by holes on TiO_2 occurs, aiding the hydroxylation of olefins. Under the optimized reaction conditions, our catalyst exhibits EG and PG production rates of $146.8 \text{ mmol}\cdot\text{g}_{\text{Pd}}^{-1}\cdot\text{h}^{-1}$ and $28.6 \text{ mmol}\cdot\text{g}_{\text{Pd}}^{-1}\cdot\text{h}^{-1}$ with liquid-phase selectivities of 63.3% and 80.0 %, respectively.

Results and discussion

Direct photocatalytic dihydroxylation of olefins by water

The photocatalyst constituted by Pd, ammonium phosphotungstic polyoxometalate (NPW) and TiO_2 was denoted as $(\text{Pd}/\text{NPW})/\text{TiO}_2$, and it was synthesized using a method previously developed by our group (see Methods for more details)²³. For referential purposes, catalysts either without Pd (i.e., NPW/TiO_2) or NPW (i.e., Pd/TiO_2), as well as catalysts with other metals (Pt, Rh, Ru, Cu, Ni) and ZnO instead of TiO_2 as host material also have been prepared. Unless otherwise specified, the metal loading in different M/NPW is kept at 0.5 wt.% and the weight ratio between M/NPW and TiO_2 is kept at 3:10.

The evaluation of different catalysts for the transformation of ethylene and water was performed in a batch reactor under light irradiation at 20 °C. Note that in addition to 5 bar ethylene, we also added 1 bar CO into the reactor to suppress the unfavorable ethylene hydrogenation side reaction, more discussion will be shown later. After 4 h of irradiation, the productivities of different catalysts are summarized in Fig. 2a. Pd/TiO_2 cannot produce EG but a small amount of ethanol (EtOH), n-butanol (n-BuOH), and acetic acid (AcOH) in the liquid phase. Interestingly, catalysts with NPW demonstrated the

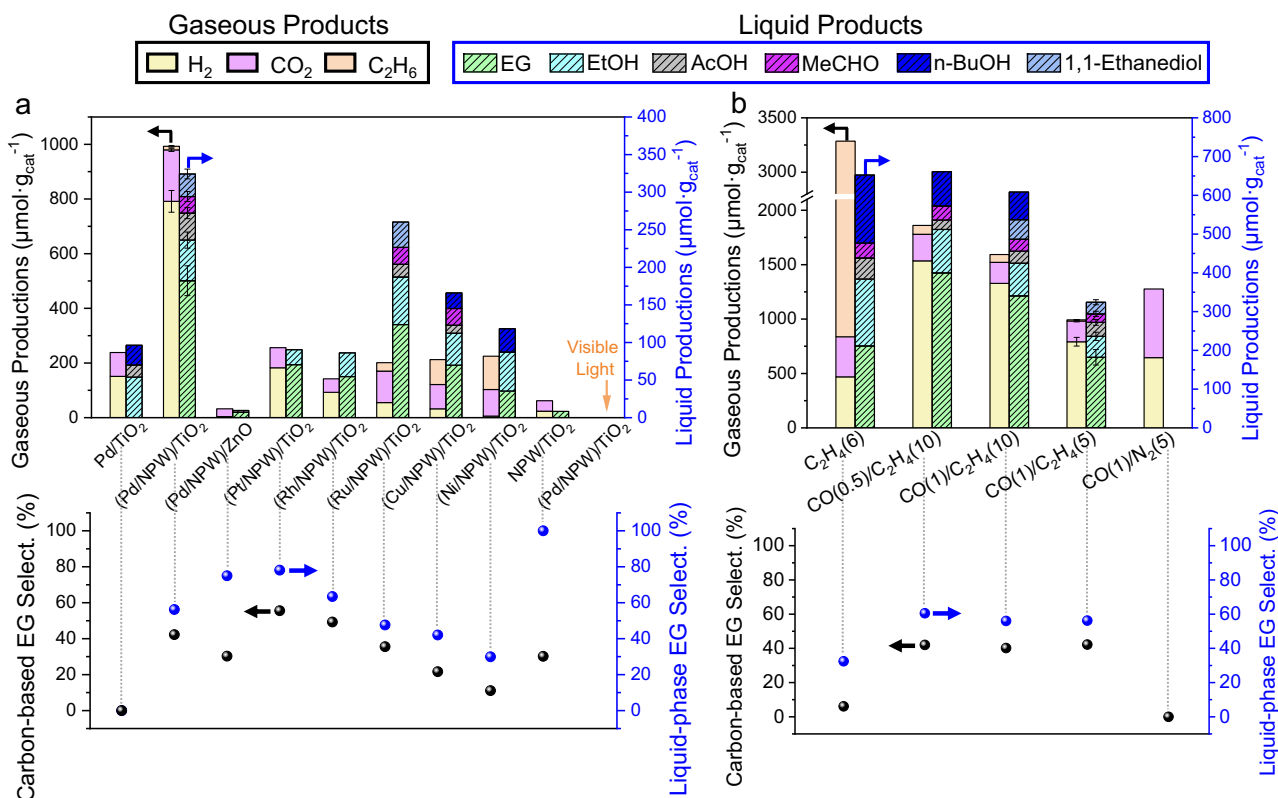


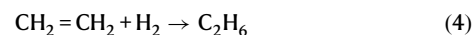
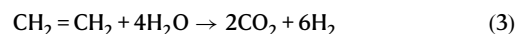
Fig. 2 | Photocatalytic transformation of ethylene and water. a Productivities and EG selectivities of different samples after 4 h irradiation. **b** Productivities and EG selectivities of (Pd/NPW)/TiO₂ under different gaseous atmospheres (unit, bar).

General reaction conditions: 50 mg catalyst, 10 mL H₂O, 20 °C, a 400 W Hg-Xe lamp as the light source. The gaseous condition in (a) is 5 bar C₂H₄ and 1 bar CO.

ability to generate EG. Among all tested samples, (Pd/NPW)/TiO₂ shows the highest EG production at 182.2 μmol·g⁻¹. The carbon-based EG selectivity and liquid-phase EG selectivity (see Methods for calculation details) of (Pd/NPW)/TiO₂ are 42.2% and 56.2%, respectively (Fig. 2a). Besides EG, the catalyst produces several additional liquid oxygenates including EtOH, AcOH, acetaldehyde (MeCHO), and 1,1-ethanediol (Supplementary Fig. 2). Presumably, ethylene hydration results in the formation of EtOH, and oxidation of ethylene/EtOH led to other oxygenates. In contrast, although (Pt/NPW)/TiO₂ achieved a higher liquid-phase EG selectivity of 78.1%, however, its EG productivity (70.6 μmol·g⁻¹) is 2 times lower compared to that of (Pd/NPW)/TiO₂. Additionally, when (Pd/NPW)/TiO₂ was irradiated with visible light (λ > 435 nm), no ethylene conversion was observed, indicating that the reaction is driven by photo-induced charge carriers from TiO₂. Moreover, ZnO is considered an alternative to TiO₂ semiconductor with a similar bandgap²⁸. The catalyst (Pd/NPW)/ZnO prepared using ZnO as a semiconductor could produce EG, however, with very low productivity. Replacing Pd in (Pd/NPW)/TiO₂ with less expensive metals such as Ru, Cu, and Ni resulted in a decrease in both the production and selectivity of EG. Notably, (Ru/NPW)/TiO₂ exhibits significantly higher performance than the other two cheap metal catalysts, and it was around 30% less active than (Pd/NPW)/TiO₂. Note that while ruthenium is three times cheaper than palladium, its worldwide production is five times smaller than that of palladium. This hinders the utilization of ruthenium catalysts on a larger scale compared to palladium.

Next, we investigated the influence of reaction conditions on EG synthesis over (Pd/NPW)/TiO₂ photocatalyst (Fig. 2b). Under the condition of 6 bar ethylene and 10 mL H₂O (without the addition of CO), after 4 h of irradiation, the gas phase contains H₂, CO₂ and ethane as products, which could be assigned respectively, to ethylene reforming with H₂O to CO₂ and H₂, and ethylene hydrogenation to ethane

(Eqs. 3–4).



In this case, the analysis of liquid products shows a similar production amount of EG to that of the conditions of 5 bar C₂H₄ and 1 bar CO. However, more side-products such as ethane, EtOH, AcOH, MeCHO, and n-BuOH were formed. Presumably, n-BuOH could be produced by ethylene dimerization to 1-butene with subsequent hydration reaction. Due to the occurrence of the above-mentioned side reactions, the carbon-based and liquid-phase selectivities of EG decreased to 6.1% and 32.4%, respectively. Optimizing the reaction conditions by increasing C₂H₄ and CO pressure to 10 bar and 0.5 bar significantly boosted the productivity and liquid-phase selectivity of EG to 400.0 μmol·g⁻¹ and 60.5%, respectively. Note that the addition of CO suppressed the formation of C₂H₆ and n-BuOH predominantly. For instance, by adding extra CO, the liquid-phase selectivity of n-BuOH decreased from 10.6% to <5.8%. Nonetheless, further increasing the partial pressure of CO to 1 bar resulted in a decrease in both EG production and selectivity. This phenomenon could be attributed to the decrease in C₂H₄ coverage of Pd sites, due to the competitive adsorption of CO. It should be noted that in the presence of both CO and C₂H₄, no coupling products of C₂H₄ and CO have been ever observed. However, higher H₂ production than the sum amount of EG and CO₂ suggests that H₂ comes partially from the reforming of C₂H₄ by H₂O (Eq. 3). Furthermore, in the absence of C₂H₄, the catalyst under CO atmosphere (with H₂O) can neither produce EG nor other liquid oxygenates, but only an equivalent amount of CO₂ and H₂ by water-gas shift reaction (CO + H₂O → CO₂ + H₂). These results suggest that CO is

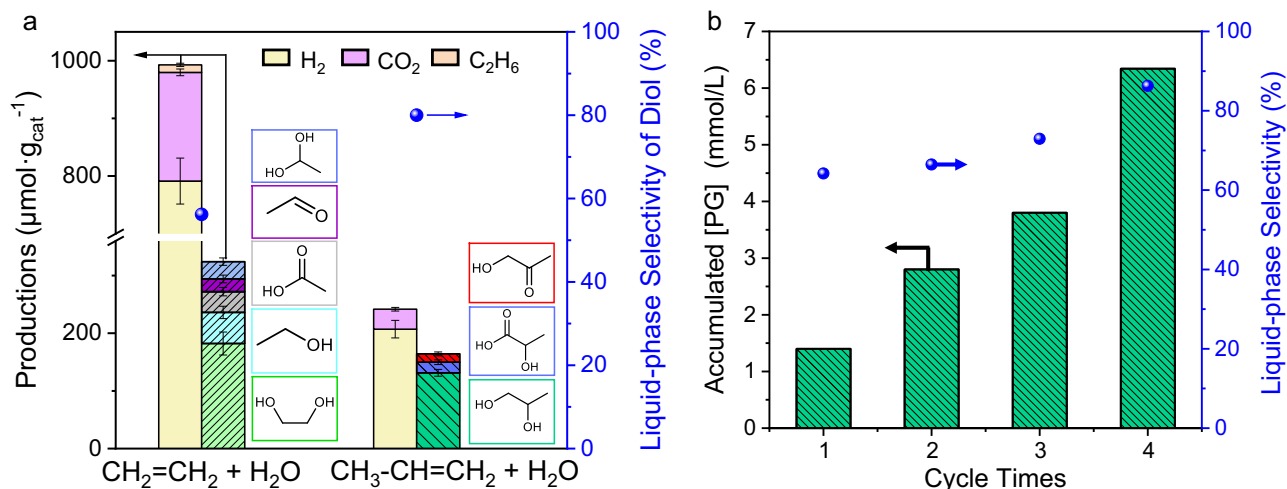


Fig. 3 | Substrate scope and stability. **a** Productivities and selectivities of liquid-phase diol in ethylene and propylene conversion over (Pd/NPW)/TiO₂ after 4 h irradiation. **b** Accumulated amount of PG over (Pd/NPW)/TiO₂ in 4 reaction cycles.

General reaction conditions: 50 mg catalyst, 10 mL H₂O, 1 bar CO and 5 bar olefins, 20 °C, a 400 W Hg-Xe lamp as the light source.

not a reactant for EG synthesis but plays an important role in suppressing undesirable ethylene reactions such as hydrogenation.

We further studied the effect of Pd loadings and the amount of catalyst on the performance of EG synthesis (Supplementary Table 1). Compared with the initial catalyst with Pd loading at 0.115 wt.%, increasing Pd loading to 0.46 wt.% can elevate the EG production to 681.5 $\mu\text{mol}\cdot\text{g}_{\text{cat}}^{-1}$ in 4 h, however, probably due to the formation of more bulk Pd atoms, the Pd-normalized activity decreased to less than a half the value. Interestingly, decreasing the loading of Pd to 0.046 wt.% brought negative effects on both catalyst- and Pd-based performance. Since lower Pd loading may improve the metal dispersion of Pd, the above structure sensitivity indicates that the formation of EG may prefer Pd ensembles with continuous Pd bonding sites. Additionally, the performance of (Pd/NPW)/TiO₂ can be further optimized by decreasing the concentration of catalyst in H₂O. Eventually, EG production and liquid-phase selectivity can be elevated to 675.2 $\mu\text{mol}\cdot\text{g}_{\text{cat}}^{-1}$ and 63.3%, respectively, corresponding to a Pd-normalized EG production rate of 146.8 $\text{mmol}\cdot\text{g}_{\text{Pd}}^{-1}\cdot\text{h}^{-1}$. Significantly, under the optimized reaction condition of (Pd/NPW)/TiO₂, an apparent quantum yield (AQY) of 22.6% was achieved under the irradiation of 360 nm monochromatic light, making it superior in reactivity among the state-of-the-art photocatalytic systems for EG synthesis (Supplementary Table 2)^{6,10,29–31}.

To further examine the performance of (Pd/NPW)/TiO₂ towards realistic applications, the photocatalytic EG synthesis of (Pd/NPW)/TiO₂ in the seawater system was first performed (Supplementary Fig. 3). Interestingly, probably the higher conductivity of seawater is more favorable for the transportation of photo-excited charge carriers, both EG production and liquid-phase selectivity of (Pd/NPW)/TiO₂ are improved in seawater. Next, we used a low power Xe lamp as a light source to mimic outdoor solar light for EG synthesis. As shown in Supplementary Table 1, entry 5, the EG production of (Pd/NPW)/TiO₂ under proximate solar light decreased by around 50% compared to that under Hg-Xe lamp (Supplementary Table 1, entry 4). However, probably due to the reduced UV intensity, the liquid-phase selectivity of EG increased from 63.3% to 74.9%.

To examine the applicability of photocatalytic olefin dihydroxylation by H₂O, we further tested the reaction of propylene with H₂O over (Pd/NPW)/TiO₂. As shown in Fig. 3a, under similar reaction conditions with ethylene dihydroxylation, after 4 h irradiation, 131.4 $\mu\text{mol}\cdot\text{g}_{\text{cat}}^{-1}$ propylene glycol (PG) was formed, corresponding to a Pd-normalized PG production of 28.6 $\text{mmol}\cdot\text{g}_{\text{Pd}}^{-1}\cdot\text{h}^{-1}$. However, unlike the production

of EG, hydroxylation of propylene proceeds with a liquid-phase selectivity to PG of 80.0% with only a small amount of lactic acid and hydroxyacetone as liquid-phase side products (Supplementary Fig. 4), and a significantly lower amount of H₂ and CO₂. Presumably, the high selectivity of PG could be attributed to the higher stability of methyl-terminated propyl radicals in comparison with ethyl radical against H₂O-induced over-oxidation. Further cyclic tests under C₃H₆ and CO atmosphere demonstrated a gradual accumulation of PG with its concentration increasing from 1.4 mmol/L to 6.3 mmol/L. During this whole process, the liquid-phase selectivity of PG remained above 70% (Fig. 3b).

Catalyst characterization

To unveil the catalytic active sites for light olefins' dihydroxylation, we performed structural characterizations of (Pd/NPW)/TiO₂ and Pd/TiO₂. The X-ray diffraction (XRD) patterns of different materials are shown in Fig. 4a. Both (Pd/NPW)/TiO₂ and NPW/TiO₂ manifest mixed crystalline phases of TiO₂ (anatase and rutile) and Keggin-type NPW hydrate (PDF#50-0305). The increased full-width at half maximum (FWHM) of NPW XRD signal for (Pd/NPW)/TiO₂ and NPW/TiO₂ confirmed the disassembling of Pd/NPW or NPW polyhedrons over the TiO₂ surface.

Consistent with the XRD results, the Z-contrast scanning transmission electron microscopy (STEM) and energy-dispersive X-ray spectroscopy (EDS) mapping analysis of (Pd/NPW)/TiO₂ show a sub-monolayer coating of Pd- and W-containing clusters on TiO₂ surface after the heat treatment of the mechanically mixed Pd/NPW and TiO₂ (Fig. 4b, c). According to our previous findings^{23,32}, these highly dispersed clusters turned out to be monomeric Pd/NPW polyhedrons. Disassembling of these acidic polyoxometalate polyhedrons has been driven by the interactions towards the surface basic sites of TiO₂. Pyridine adsorption FT-IR spectroscopy confirms the presence of Brønsted acid sites on (Pd/NPW)/TiO₂ that are not completely neutralized by ammonia while these sites are not observed over Pd/TiO₂ (Supplementary Fig. 5).

Characterization by XRD of (Pd/NPW)/TiO₂ after ethylene dihydroxylation reactions showed a slight decrease in the peak intensity of Pd/NPW relative to TiO₂ (Supplementary Fig. 6). As the STEM analysis of the spent catalyst exhibits an improved coverage of Pd/NPW clusters on TiO₂ (Supplementary Figs. 7 and 8), these combined results indicate a further increase in the dispersion of Pd/NPW clusters on the surface of TiO₂ during photocatalysis. This is consistent with its good photocatalytic stability in cyclic tests.

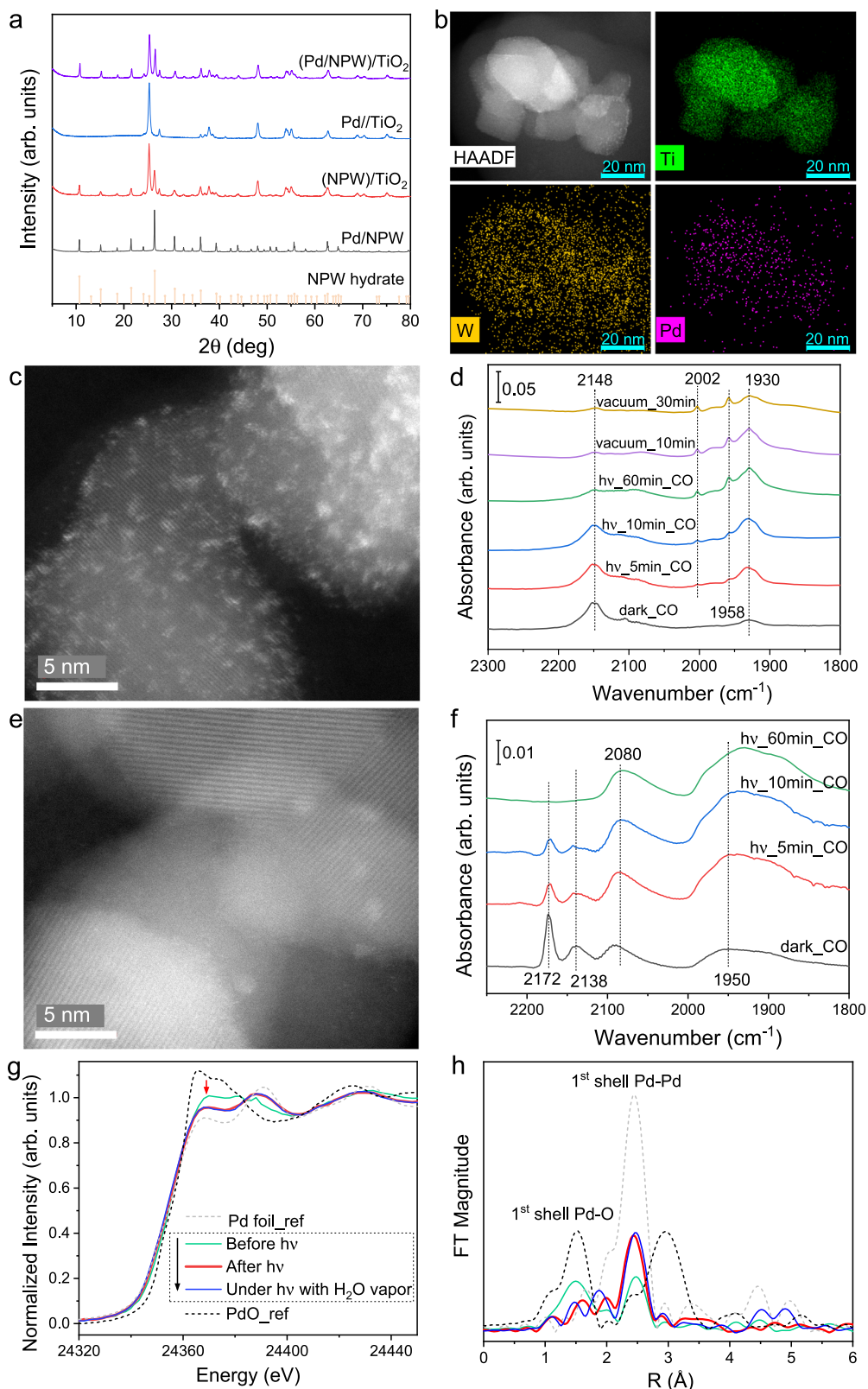


Fig. 4 | Structural characterizations of catalysts. **a** XRD patterns of different catalysts. **b** HAADF-STEM and corresponding EDS-mapping images (Pd/NPW)/TiO₂. **c** High-resolution HAADF-STEM image of (Pd/NPW)/TiO₂. **d** In situ FT-IR spectra of (Pd/NPW)/TiO₂ under CO adsorption and light irradiation. **e** HAADF-STEM image of

Pd/TiO₂. **f** In situ FT-IR spectra of Pd/TiO₂ under CO adsorption and light irradiation. **g** Pd K edge XANES and **h** FT EXAFS spectra of (Pd/NPW)/TiO₂ under continuous different treatments. Note that the color of different curves in **(g)** are consistent with that in **(h)**.

We further performed in-situ CO-probe Fourier transform infrared (FT-IR) spectroscopy analysis to examine the dispersion state of Pd on NPW clusters. As shown in Fig. 4d, the adsorption of CO on (Pd/NPW)/TiO₂ in the dark exhibit one main absorption band at 2148 cm⁻¹, assigning to linear CO adsorption (CO_{ads}) over cationic Pd²⁺ in the ion exchange position of polyoxometalate anion³³. Upon light irradiation, this band gradually disappears and is substituted by CO_{ads} band at 1930 cm⁻¹ with small peaks at 2002 and 1958 cm⁻¹. In general, the peaks at 1930 and 1958 cm⁻¹ are assigned to bridge bonded CO with different configurations of metallic Pd clusters and the peak at 2002 cm⁻¹ can be assigned to linearly adsorbed CO molecules³⁴. The narrow peaks of CO adsorption and absence of the peaks with a frequency lower than 1900 cm⁻¹ (i.e., the multiple bonded CO adsorption over Pd nanoparticles) indicate that most of Pd species present as Pd clusters with several atoms. It is interesting to note that a decrease in Pd content to 0.046 wt.% leads to the appearance of the dominant band at 2080 cm⁻¹ after light treatment (Supplementary Fig. 9), corresponding to the linear CO adsorbed over isolated Pd atoms³⁴. This result further confirms the above-mentioned requirement of clusters in EG synthesis.

In comparison, the Pd/TiO₂ reference sample exhibited a morphology of uniformly distributed PdO_x clusters at around 2 nm on TiO₂ surface (Fig. 4e). CO-probe FT-IR analysis of Pd/TiO₂ catalyst demonstrates the presence of the narrow bands at 2172 and 2138 cm⁻¹ assigned to carbonyl Pd²⁺(CO)₂ in PdO with less intensive broad bands at 2080 and 1950 cm⁻¹ due to the presence of linear and multiple bonded CO over metallic Pd clusters (Fig. 4f)^{33,34}. Treatment by light induces a reduction of Pd with a decrease in the intensity of CO bands at 2172 and 2138 cm⁻¹ and an increase in the intensity of the bands at 2080 and 1950 cm⁻¹, indicating the reduction of PdO_x clusters into metallic state.

To further investigate the structural evolution of Pd species of (Pd/NPW)/TiO₂ under light irradiation, we performed in situ X-ray absorption spectroscopy studies on Pd K edge. Before the light treatment, the white line of X-ray absorption near-edge spectrum (XANES) of (Pd/NPW)/TiO₂ showed a median intensity among reference Pd foil and PdO, indicating a partially oxidized state of Pd (Fig. 4g). Interestingly, after light irradiation, the XANES white line feature of (Pd/NPW)/TiO₂ shifted towards Pd foil (highlighted by red arrow). Afterwards, introducing H₂O vapor under light irradiation did not bring noticeable modifications to XANES profile. The XANES results are consistent with those previously obtained for Pd catalysts under the conditions of methane coupling³⁵. The reduction of Pd after light treatment resulted from the directional migration of photo-induced electrons from TiO₂ to Pd/NPW clusters, a similar phenomenon of Pd reduction has been witnessed in the previous CO-probe FT-IR analysis. XPS analysis also shows a partial reduction of Pd after reaction (Supplementary Fig. 10). Notably, the subsequent unchanged oxidation state of Pd in the presence of both H₂O vapor and light irradiation suggests that the hydroxylation of light olefins may not involve a H₂O-induced redox cycle of Pd. Following the XANES, the Fourier transform of extended X-ray absorption fine structure (EXAFS) of (Pd/NPW)/TiO₂ demonstrated an elevation of Pd-Pd coordination after light irradiation (Fig. 4h). Quantitative EXAFS curve fitting suggests the Pd-Pd coordination number of (Pd/NPW)/TiO₂ increased from 3.0 (before hv) to 5.5 (after hv) (Supplementary Table 3), further confirming the reduction of oxidized Pd clusters on NPW. Overall, the above characterization results implied that light could induce the formation of Pd clusters (Pd_n) with certain metallic properties. The polyoxometalate, on the other hand, plays a key role in the stabilization of Pd clusters over the surface of TiO₂.

Reaction mechanism of photocatalytic dihydroxylation of light olefins

We first identified the photo-excited charge transfer direction between TiO₂ and Pd/NPW clusters. By employing AgNO₃ as an electron scavenger under light irradiation, the locations of the in situ formed Ag NPs on the photocatalyst can be used as indicators of the electron-

enriched sites³⁶. As shown in Supplementary Fig. 11, high-resolution STEM and EDX-mapping images clearly demonstrate that Ag NPs with a diameter of around 5 nm are formed in close contact with Pd/NPW clusters. This indicates that the dominant electron injection direction is from TiO₂ to Pd/NPW rather than the opposite. Then, by replacing H₂O with CH₃CN in the C₂H₄ transformation process, the H₂ production of (Pd/NPW)/TiO₂ decreased to a negligible level, and no EG was produced (Supplementary Fig. 12). Overall, these results demonstrated that the photo-excited electrons transferred directionally from TiO₂ to Pd/NPW clusters and were used for H₂ production via H₂O reduction.

Subsequently, the function of the Pd/NPW cluster cocatalyst in the separation and transfer dynamics of photo-excited charge carriers was investigated. The steady-state photoluminescence (PL) emission spectra of representative TiO₂, Pd/TiO₂, and (Pd/NPW)/TiO₂ excited by a 320 nm laser are shown in Supplementary Fig. 13. Clearly, all three samples exhibit one broad peak from 350 nm to 600 nm, representing the radiative emission of charge carrier recombination³⁷. Compared with pristine TiO₂ and Pd/TiO₂, the significantly quenched PL signal of (Pd/NPW)/TiO₂ suggests that the presence of Pd/NPW clusters effectively suppresses charge carrier recombination.

To gain deeper insight into the dynamics of photo-excited charge carriers, we subsequently performed femtosecond transient absorption (fs-TA) spectroscopy measurements on these three samples. As shown in Supplementary Fig. 14a-c, under the excitation of a 266 nm laser, all three samples exhibit broad positive absorption features from 600 to 780 nm on the picosecond to nanosecond scale, attributed to the excited-state absorption (ESA) of charge carriers³⁸. The kinetic ESA decay traces at 760 nm for different samples and the related decay curve fitting results are shown in Supplementary Fig. 14d and Supplementary Table 4. Remarkably, the estimated τ₃ (12.7 ns) and the corresponding portion A₃ (39.1%) of (Pd/NPW)/TiO₂ are significantly increased compared with TiO₂ (τ₃ = 8.19 ns, A₃ = 30.7%) and Pd/TiO₂ (τ₃ = 8.78 ns, A₃ = 26.7%). This indicates that the presence of Pd/NPW clusters prolongs the lifetime and enhances the abundance of charge carriers through long-lived charge trapping, consistent with the steady-state PL results mentioned above.

We have considered several possible mechanisms for dihydroxylation of olefins by water over the catalyst. First, the reaction could proceed in a way similar to OsO₄ via a Mars-Van Krevelen type mechanism by the reaction of olefins with the oxygen of polyoxometalate and further regeneration of oxygen by water with the production of hydrogen³⁹. This route has been studied using ¹⁷O solid-state NMR spectroscopy of the (Pd/NPW)/TiO₂ samples after the reaction with H₂¹⁶O water or with the water enriched by 10% with the ¹⁷O isotope (Supplementary Fig. 15). The ¹⁷O MAS NMR spectrum of initial (Pd/NPW)/TiO₂ contains three low intensive signals at ca. 40, 400 and 540 ppm produced by internal and external ¹⁷O atoms of NPW ions and TiO₂ with natural ¹⁷O-isotope content (0.038%)^{40,41}. The ethylene dihydroxylation process with H₂¹⁷O does not lead to any changes in ¹⁷O NMR signal intensities. So, no oxygen exchange between NPW ions and water occurs under the reaction conditions. Additionally, XPS analysis of (Pd/NPW)/TiO₂ before and after the photocatalytic reaction showed a similar profile in the W 4f region (Supplementary Fig. 16), further indicating that the dihydroxylation of ethylene does not involve the reduction of tungsten species. Thus, the dihydroxylation of olefins does not involve oxygen from the framework of NPW or TiO₂. Only water provides therefore oxygen for dihydroxylation.

Then, we speculate that the dihydroxylation of light olefins might proceed through the direct coupling of olefins with H₂O-derived hydroxyl radicals (•OH). To investigate this scenario, we begin with the in-situ electron paramagnetic resonance (EPR) analysis to probe possible radical species during ethylene dihydroxylation. Under simulated reaction conditions of ethylene dihydroxylation, with (Pd/NPW)/TiO₂ as a catalyst and 5,5-dimethyl-1-pyrroline N-oxide (DMPO) as a spin

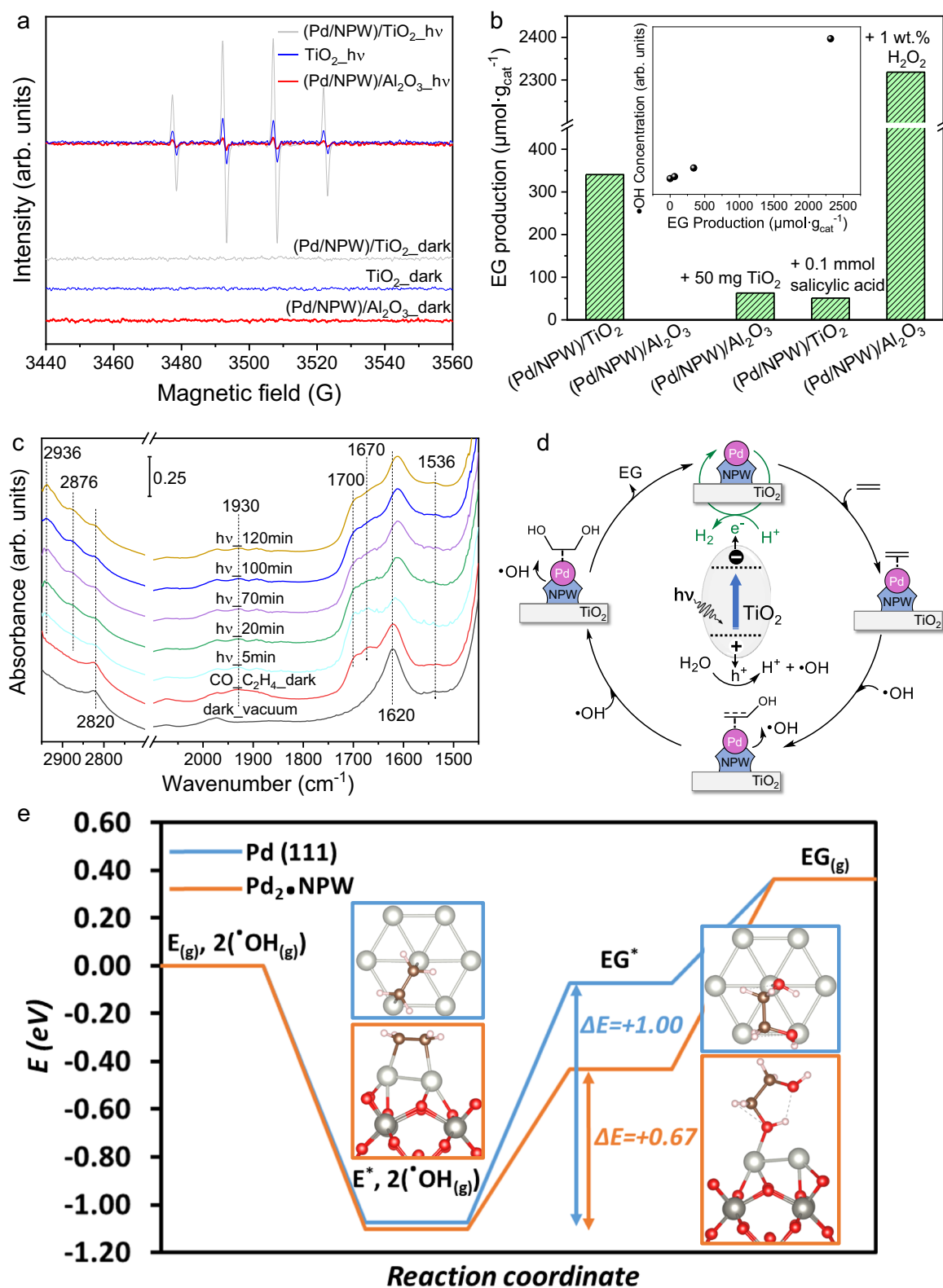


Fig. 5 | Mechanistic studies of photocatalytic ethylene dihydroxylation. **a** in situ EPR spectra of different samples under simulated reaction conditions with or without light irradiation. **b** EG production comparison between different catalysts under designated conditions. Inset image shows the correlation between EG production of different catalysts with their •OH concentration as probed by EPR analysis. **c** in situ FT-IR spectra of (Pd/NPW)/TiO₂ under simulated reaction conditions with or without light irradiation. **d** Proposed reaction mechanism over a simplified

catalyst model with TiO₂ support and NPW stabilized Pd clusters. **e** Reaction energy diagram related to ethylene (E) transformation into ethylene glycol (EG) at metallic Pd (111) surface (in blue) and NPW embedded Pd cluster (Pd₂·NPW) (in orange), with related reaction energies in eV (ΔE). “E*” and “EG*” represent adsorbed ethylene and ethylene glycol, respectively. E* and EG* ball and stick models are represented in their most stable adsorption mode at Pd (111) and Pd₂·NPW. Color code: light gray Pd, dark gray W, red O, pink H, brown C.

trapping agent, strong signals representing $\bullet\text{OH}$ were instantly detected upon light irradiation (Fig. 5a). In contrast, pure TiO_2 exhibited a weak $\bullet\text{OH}$ signal while $(\text{Pd}/\text{NPW})/\text{Al}_2\text{O}_3$ could hardly produce $\bullet\text{OH}$ or any other species.

To further confirm the essential roles of $\bullet\text{OH}$ in dihydroxylation, additional experiments were performed. As different to TiO_2 , Al_2O_3 does not produce charge carriers under UV irradiation, therefore, $(\text{Pd}/\text{NPW})/\text{Al}_2\text{O}_3$ is inactive in converting C_2H_4 and H_2O into EG (Fig. 5b). Interestingly, mixing equivalent weights of $(\text{Pd}/\text{NPW})/\text{Al}_2\text{O}_3$ and TiO_2 resulted in a relatively small EG production of $62.8 \mu\text{mol}\cdot\text{g}^{-1}$ in 4 h. Probably due to the difficulty in transferring charge carriers and radicals, the mixed sample is several times less active than $(\text{Pd}/\text{NPW})/\text{TiO}_2$ (Fig. 5b). Also, although TiO_2 and ZnO have similar properties as semiconductors, yet the amount of hydroxyl radicals and catalytic efficiency of $(\text{Pd}/\text{NPW})/\text{TiO}_2$ is significantly higher than $(\text{Pd}/\text{NPW})/\text{ZnO}$ (Fig. 2a and Supplementary Fig. 17). According to Wong et al. the formation rate of $\bullet\text{OH}$ on TiO_2 in an aqueous solution is much faster than other semiconductors such as of ZnO due to slower recombination of the photo-generated electrons and holes over TiO_2 , leading to efficient water oxidation to $\bullet\text{OH}$ radicals⁴². It indicates the advantages of TiO_2 responsible for Pd/NPW dispersion and charge carriers' utilization. As H_2O_2 could be decomposed into $\bullet\text{OH}$ under UV light irradiation (Supplementary Fig. 18), the originally inactive $(\text{Pd}/\text{NPW})/\text{Al}_2\text{O}_3$ showed a great improvement of EG production (up to $2318 \mu\text{mol}\cdot\text{g}^{-1}$ in 4 h) when 1% H_2O_2 aqueous solution was used for the reaction. In contrast, adding salicylic acid as a reactive oxygen scavenger drastically reduced the EG production of $(\text{Pd}/\text{NPW})/\text{TiO}_2$ down to $51.0 \mu\text{mol}\cdot\text{g}^{-1}$ in 4 h. Importantly, by correlating EG productivities and the detected $\bullet\text{OH}$ concentration as probed by EPR analysis (Fig. 5b, inset), the resulted linear correlation demonstrated that the H_2O derived $\bullet\text{OH}$ radicals are indeed, acting directly as reactive species in transforming ethylene into EG. The $\bullet\text{OH}$ radicals seem to be generated over TiO_2 through the reaction of photo-generated holes with H_2O . Meanwhile, hydrogen evolution occurs over NPW stabilized Pd clusters by accepting photo-generated electrons.

It should be noted that the presence of NPW does not directly contribute to the formation of either $\bullet\text{OH}$ or H_2 (Supplementary Figs. 19 and 20). However, NPW could be involved in the transfer of $\bullet\text{OH}$ radicals to ethylene or the adsorption of ethylene by protonation in the proximity of Pd. Indeed, as shown in Supplementary Fig. 21, the reference test of ethylene dihydroxylation using Pd/TiO_2 with HPW in the aqueous solution produces a significant amount of EG. At the same time, the test of Pd/TiO_2 with H_2SO_4 does not show noticeable EG production, indicating that the effect of Brønsted acidity of NPW could be excluded (Supplementary Fig. 5). Thus, the role of NPW could be, besides the stabilization of Pd clusters and prolonging the lifetime of photo-excited charge carriers, the transfer of $\bullet\text{OH}$ radicals to adsorbed ethylene.

Subsequently, we employed in situ FT-IR spectroscopy to have a deep insight into the evolution of surface intermediates. As shown in Fig. 5c, under dark and vacuum, $(\text{Pd}/\text{NPW})/\text{TiO}_2$ manifested two peaks at 2820 cm^{-1} and 1620 cm^{-1} , assigning to ammonium ions and OH bending of H_2O , respectively^{43,44}. Introducing mixed CO and C_2H_4 (1 bar, 1/10, v/v) gas into the chamber led to the emergence of absorption bands at 1930 cm^{-1} , 1700 cm^{-1} , and 1670 cm^{-1} . The former signal belongs to the bridge-bonded CO at Pd clusters, while the latter two signals could be assigned to the stretching vibration of carbonyl and vinyl groups of adsorbed acetaldehydes and vinyl alcohol, respectively⁴⁵. The formation of these two species might be the cause of the oxidation of ethylene by oxygen adsorbed over Pd clusters. Yet, their gradual decomposition (i.e., first increase then decrease) upon light irradiation suggests both are not key intermediates in EG synthesis. Notably, under light irradiation, the signal at 1536 cm^{-1} which belongs to the C=C stretching vibration of π -bonded ethylene emerged and increased simultaneously with the signal of EG at 2936 cm^{-1} and 2876 cm^{-1} ^{43,46}. Together with the gradually weakening

H_2O signal at 1620 cm^{-1} , these results suggest that the formation of EG might proceed via the coupling of H_2O -derived $\bullet\text{OH}$ with oriented-bonded ethylene at Pd_n sites. In contrast, it is interesting to note that the same light treatment of ethylene and CO over Pd/TiO_2 leads to the appearance of the bands at 1565 cm^{-1} , 1440 cm^{-1} and 1358 cm^{-1} (Supplementary Fig. 22), related to π -bonded C_2H_4 , di- δ -bonded C_2H_4 , and ethynylidyne, respectively⁴⁶. However, no EG but the absorption band at 2860 cm^{-1} which belongs to the C-H vibration of ethanol was noticed along light irradiation.

Based on the above understanding, the reaction mechanism of EG synthesis via photocatalytic ethylene dihydroxylation by $\bullet\text{OH}$ radicals was proposed and depicted in Fig. 5d. First, under UV light irradiation, the photo-excited electrons from TiO_2 were transferred to NPW-stabilized Pd_n clusters, while the photo-excited holes reacted directly with H_2O to form H^+ and $\bullet\text{OH}$. Subsequently, over oxygen-coordinated Pd_n site on NPW clusters, besides the hydrogen evolution reaction ($\text{H}^+ + \text{e}^- \rightarrow 1/2\text{H}_2$), ethylene was adsorbed via a π -bonded model, followed by the coupling of $\bullet\text{OH}$ transferred from the adjacent NPW to produce EG. Note that, we assume CO acted as a site-blocking agent that maintained the glycols' selectivity by suppressing subsequent olefins' hydrogenation side reactions.

The superior catalytic properties of $(\text{Pd}/\text{NPW})/\text{TiO}_2$ relative to Pd/TiO_2 are consistent with band structure analysis and DFT calculations. Indeed, though $(\text{Pd}/\text{NPW})/\text{TiO}_2$ exhibits a similar band gap energy to TiO_2 and Pd/TiO_2 according to their Tauc plots (Supplementary Fig. 23), yet the valence band (VB) XPS analysis suggests that $(\text{Pd}/\text{NPW})/\text{TiO}_2$ possesses more positive VB position relative to TiO_2 and Pd/TiO_2 (Supplementary Figs. 24 and 25), which makes the photo-generated holes from $(\text{Pd}/\text{NPW})/\text{TiO}_2$ more reactive in H_2O oxidation to produce $\bullet\text{OH}$. Additionally, by constructing Pd (111) and Pd_2 -NPW as simplified models to represent Pd species in Pd/TiO_2 and $(\text{Pd}/\text{NPW})/\text{TiO}_2$, respectively, theoretical calculation in Fig. 5e shows that ethylene to EG transformation reaction energy is significantly higher at Pd (111) facet compared to Pd_2 -NPW cluster, with values of 1.00 and 0.67 eV, respectively. In our model, we consider a concerted mechanism with two different $\bullet\text{OH}$ radicals simultaneously attacking the vicinal C atoms. While ethylene adsorption energy is similar on both surfaces, EG is considerably more stable at small Pd clusters over NPW than at metallic Pd, hence impacting the catalytic properties of the two materials.

In summary, we demonstrated a photocatalytic dihydroxylation route to transform ethylene and propylene by their reaction with water directly into glycols and hydrogen at room temperature. The catalyst developed for this process is constituted by TiO_2 support and Pd clusters stabilized by phosphotungstic polyoxometalate clusters. In the presence of CO as a site-blocking agent to suppress the unfavorable hydrogenation side-reactions, we achieved liquid-phase selectivities of 63.3% and 80.0% towards EG and PG, respectively. Combined spectroscopic and theoretical results suggest that the dihydroxylation of olefins takes place via the direct coupling of H_2O -derived $\bullet\text{OH}$ with π -bonded ethylene on polyoxometalate stabilized Pd clusters.

Methods

Chemicals

Tetraammineplatinum(II) nitrate ($[\text{Pt}(\text{NH}_3)_4](\text{NO}_3)_2$, 99.99%), aluminum oxide (Al_2O_3) were purchased from Alfa Aesar. Other chemicals including tetraamminepalladium(II) nitrate ($[\text{Pd}(\text{NH}_3)_4](\text{NO}_3)_2$, 10wt.% in H_2O), rhodium(III) nitrate hydrate ($\text{Rh}(\text{NO}_3)_3\cdot x\text{H}_2\text{O}$, -36% rhodium basis), copper(II) nitrate trihydrate ($\text{Cu}(\text{NO}_3)_2\cdot 3\text{H}_2\text{O}$), ruthenium(III) chloride (RuCl_3 , Ru content: 45-55%), nickel nitrate hexahydrate ($\text{Ni}(\text{NO}_3)_2\cdot 6\text{H}_2\text{O}$), phosphotungstic acid hydrate ($\text{H}_3[\text{P}(\text{W}_3\text{O}_{10})_4]\cdot x\text{H}_2\text{O}$, abbreviated as HPW, reagent grade), ammonium nitrate (NH_4NO_3 , ACS reagent, $\geq 98\%$), titanium dioxide (TiO_2 , P25, $\geq 99.5\%$ trace metals basis), ammonia aqueous solution (NH_4OH , > 25 %), deuterium oxide (D_2O , 99.9 atom % D), dimethyl sulfoxide ($(\text{CH}_3)_2\text{SO}$, DMSO, anhydrous, $\geq 99.9\%$), ethylene glycol ($\text{HOCH}_2\text{CH}_2\text{OH}$, $\geq 99\%$), 1,2-propanediol

(CH₃CH(OH)CH₂OH, ACS reagent, ≥99.5%), ethanol (CH₃CH₂OH, ≥99%), 1-butanol (CH₃(CH₂)₃OH, ACS reagent, ≥99.4%), acetic acid (CH₃COOH, ACS reagent, ≥99.8%), acetaldehyde (CH₃CHO, ACS reagent, ≥99.5%), were all purchased from Sigma Aldrich. Seawater was obtained from Cancale Bay of France. All chemicals were used as received without further purification.

Synthesis of catalysts

The synthesis of ternary phased (Pd/NPW)/TiO₂ followed a similar protocol as our previous works²³. In a typical process, solution A was firstly prepared by adding 50 μL 10 wt.% [Pd(NH₃)₄](NO₃)₂ aqueous solution to 5 mL NH₄NO₃ solution (0.075 M). Then, under vigorous stirring at room temperature, solution A was added dropwise into solution B (5 mL HPW solution, 0.025 M). After 30 min stirring, the precipitate (i.e., Pd/NPW) was collected by centrifuge and washed 2 times with deionized (DI) water. After drying, 60 mg of Pd/NPW and 200 mg of TiO₂ were thoroughly mixed by grinding, and then, the mixed powder was aged in an 80 °C oven for 24 h. At last, after a 2 h calcination at 250 °C in static air, the final ternary-phased composite of (Pd/NPW)/TiO₂ was obtained. The composites with different group VIII metals (i.e., (M/NPW)/TiO₂, M = Pt, Rh, Ru, Ni, Cu), without group VIII metal, or support (i.e., Al₂O₃ and ZnO) were prepared similarly, simply by replacing either the metal precursor or support to the designated one. Moreover, referential Pd/TiO₂ was prepared via the strong electrostatic adsorption (SEA) method⁴⁷, with a theoretical Pd loading of 0.1 wt.%. Typically, 600 mg TiO₂ was dispersed in diluted ammonia solution (50 mL NH₄OH + 10 mL H₂O) and followed with sonication treatment. Then, 10 wt.% aqueous solution of [Pd(NH₃)₄](NO₃)₂ in ammonia (20 μL in 5 mL) was added dropwise to the above TiO₂-ammonia suspension under vigorous stirring at room temperature. After 2 h stirring, the catalyst precursor was washed by DI water and dried at 80 °C overnight. Lastly, the dried sample was further calcined at 250 °C in static air for 2 h.

Catalyst characterization

The X-ray powder diffraction (XRD) patterns of catalysts were collected using the PANalytical Empyrean X-ray diffractometer with a Cu-Kα radiation source (40 kV and 30 mA). The ultraviolet–visible diffuse reflectance spectroscopy (UV-vis DRS) analysis was performed on a PerkinElmer Lambda 650S spectrometer, with an integrating sphere covered with BaSO₄ as a reference. The Tauc plots were derived from UV-vis DRS spectra by correlating (αhν)² versus hν. The scanning transmission electron microscopy (STEM) was performed on a TITAN Themis 300 S/TEM microscope equipped with a probe aberration corrector and monochromator, allowing spatial resolution of 70 pm and energy resolution of 150 meV, a super-X windowless 4 quadrant SDD (silicon drift detector) detection system for STEM-EDX mapping and several annual dark field detectors. The measurements were performed with a spot size of about 500 pm, a semi-convergence angle between 20 mrad, and a probe current of approximately 100 pA. For the HAADF images, collection angles were chosen between 50 and 200 mrad²³. The in-situ Pd K-edge X-ray absorption spectra were recorded at the SuperXAS beamline station of the Swiss Light Source (Villigen, Switzerland). Prior to the XAS measurements, the calcinated catalyst (sieved between 60–140 mesh) was packed between two layers of quartz wool within a quartz capillary (O.D. = 2 mm). Spectra processing and analysis was carried out with the Athena software package⁴⁸. The energy scale was calibrated by setting the first inflection point of the Pd metal foil taken as 24350 eV. EXAFS were extracted using the AUTOBK algorithm employing a spline in the range of 0 to 15.0 Å⁻¹ having an R_{bkg} of 1.1. The FEFF6 code^{49,50} was used for scattering path generation, and multi (k¹, k², k³)-weighted fits of the data were carried out in r-space over an r-range of 1–3.2 Å and k-range of 3–13 Å⁻¹ unless otherwise specified. The S₀² value was set to 0.9, and a global E₀ was employed with the initial E₀ value set to the first inflection point of the rising edge. Single scattering paths were fit in terms of a Δ_{reff} and σ², which represent the

deviation from the expected interatomic distances and the structural disorder, respectively⁵¹. Co-linear Pd-CO paths were fit with a common Δ_{reff} and σ². To assess the goodness of the fits both the R_{factor} (%R) and the reduced χ² (χ²_r) were minimized, ensuring that the data was not over-fit. Best fit models were determined using a grid search with fixed values for path coordination numbers (N) by employing Larch, the Python implementation of Artemis^{52,53}. In-situ FT-IR spectra were recorded on a Nicolet 6700 FT-IR Spectrometer (Thermo Fisher Scientific) with a mercury cadmium telluride detector. Before the analysis, 40 mg catalyst was compressed into a wafer with a diameter of 13 mm. Then, the catalyst wafer was transferred into the in-situ reaction cell and was degassed under a high vacuum condition (<10⁻⁵ torr) at room temperature for 60 min. Afterwards, mixed CO and C₂H₄ (1 bar, 1/10, v/v) gas was introduced into the reaction cell, such condition was maintained in the dark for 30 min. Subsequently, the catalyst wafer was irradiated vertically by a spot light source (Hamamatsu L9588 LightningCure) for 2 h. Note that once the catalyst wafer was loaded into the reaction cell, the FT-IR spectrum was recorded continuously (32 scans at a resolution of 4 cm⁻¹). CO adsorption over FT-IR analysis was conducted similarly, simply introducing 1 bar CO into the in-situ reaction cell and followed with 60 min light irradiation and vacuum treatment. Pyridine adsorption FT-IR analysis was performed by adding 5 torr pyridine into the in-situ reaction cell and followed with vacuum treatment. The analysis of paramagnetic species has been performed by Continuous-Wave Electron Paramagnetic Resonance (CW-EPR). These experiments were performed on a Bruker ELEXSYS E500 spectrometer operating in X-band (9.5 GHz). The spin trapping experiments are performed with [DMPO] = 80 mM, microwave power of 10 mW, modulation amplitude of 0.2 G, a conversion time of 5 ms and 100 scans. An EPR quick pressure tube is used to work under CO/C₂H₄ (1:10, v/v, 5 bar) atmosphere. A spot light source (Hamamatsu L9588 LightningCure) was used for the illumination. Data were simulated using WinSim software. The PL spectra of different samples were measured with 320 nm excitation (HR Labram, Horiba Scientific). To be able to compare precisely the PL intensities of samples, the measured spectra were normalized with respect to the Raman peaks at 329.3, 330.5, and 331.8 nm. The fs-TA measurements were conducted using the Helios pump-probe transient absorption spectrometer system (Ultrafast Systems, USA) with the femtosecond laser from the Spitfire Pro regenerative amplified Ti:sapphire laser system (Spectra Physics, USA)⁵⁴. The 266-nm laser light with 120-fs pulse wide was subsequently split into two beams, one as the pump beam and another one as the probe beam. The pump beam passed through a harmonic resonator to generate the 266-nm pump beam (the third harmonic of the fundamental 800 nm), whereas the probe beam passed through a sapphire crystal and generated a white-light continuum (450 – 800 nm). The time-delayed probe beam was controlled by the optical delay rail with a maximum temporal delay at 7000 ps. It would pass through the samples and the signals were then collected by the detector. A reference probe beam was also used to optimize signal-to-noise ratio. The aqueous sample suspensions (around 0.0625 mg/mL) were prepared with an absorbance of approximately 1.0 at 400 nm and measured in a 2-mm path-length quartz cuvette, and the films were directly fixed on the sample holder⁵⁵. The spectrometric data were recorded in a 3D wavelength-time-absorbance matrix. The subtraction of background, the subtraction of scattering light, and chirp correction were done for all the data before analysis. The principal components were ensured by singular value decomposition (SVD), and then the global fitting was carried out with the selected principal components and exponential function using the sequential kinetics scheme based on the fs-TA spectra by Surface Explorer 4.5. The single-wavelength kinetic fitting was carried out (1) by Surface Explorer 4.5. For XPS, we used a Kratos Axis Ultra DLD photoelectron spectrometer using monochromatic Al Kα (1486.7 eV) X-ray irradiation. High-resolution spectra were collected after loading the samples in an ultrahigh vacuum with an analysis area of 300 – 700 μm and a 20 eV pass energy.

Photocatalytic tests

The photocatalytic light olefins' dihydroxylation reactions were performed in a 100 mL batch reactor, using a Mercury-Xenon arc lamp (Newport, 200 – 500 W) as the light source. The optical power density was measured as 279 mW/cm² and was kept consistently in this study. In a typical batch, 50 mg catalyst was firstly mixed in 10 mL DI water by sonication. After the catalyst water suspension was transferred into the reactor, the reactor was evacuated by a vacuum pump and charged sequentially with CO and light olefins (C₂H₄, C₃H₆) to a designated pressure (6 – 11 bar, absolute pressure). For comparison purposes, photocatalytic reaction was also performed in a mixed CO (1 bar) + N₂ (5 bar) atmosphere. Throughout the reaction, the catalyst-water suspension was magnetically stirred, and the reaction temperature was kept at 20 °C by a circulating water machine with a constant temperature. After photocatalytic reactions, the gaseous products were analyzed by a gas chromatograph (Agilent 8860) equipped with a PoraBOND Q and a ShinCarbon ST 100/120 columns, as well as a thermal conductive detector and a flame ionized detector. The liquid product was analyzed by ¹H nuclear magnetic resonance (NMR) spectroscopy, by mixing 0.5 mL filtered liquid sample with 0.1 mL DMSO/D₂O solution (1/2000, v/v, DMSO is the internal standard). The carbon-based selectivities of EG and PG were calculated based on the carbon numbers of all carbonaceous products (Eqs. 5 and 7). The liquid-phase selectivities of EG and PG were calculated based on the mole numbers of all liquid products (Eqs. 6 and 8). For the cyclic experiments, after the gaseous- and liquid-phase sampling at the end of each cycle, the reactor was sealed, evacuated under vacuum, and refilled with 1 bar CO and 5 bar propylene for the next cycle.

Reactive oxygen species (ROS) scavenging test

Salicylic acid was used as a scavenging agent for hydroxyl radicals (•OH) removal. The conditions of the reaction were similar to those in previous reports^{56,57}: 50 mg (Pd/NPW)/TiO₂, 10 mL H₂O with 0.1 mmol salicylic acid, 1 bar CO and 10 bar C₂H₄, 20 °C, and a 400 W Hg-Xe light source.

NMR studies

The solid-state ¹⁷O NMR spectra were recorded on 18.8 T BRUKER AVANCE-NEO NMR 800 SB spectrometer. Triple-channel 3.2 mm Phoenix MAS NMR probe with rotation of 22727 Hz was used. The samples were packed into a 3.2 mm diameter zirconia rotor under an oxygen-free and water-free argon atmosphere and spun at the magic angle in the probe. Chemical shifts were attributed to distilled H₂¹⁷O (10% ¹⁷O enrichment).

¹⁷O MAS NMR spectra were obtained with preliminary double-frequency sweep technique (DFS) of central transition signal approval (duration 1 ms, sweep 200 kHz, B₁ – 71 kHz) and following direct polarization (90-degree pulse – 2.4 μs, B₁ – 104.2 kHz) with echo-train QCPMG acquisition synchronized with magic angle spinning (DFS-DP-MAS-QCPMG). Number of echos in QCPMG – 48, half-duration of echo – 216 μs, recycle delay – 2 s, number of scans – 40000, total duration 22.2 h. The Fourier transformation of the summed echos was performed with preliminary apodization by the Gaussian window function (GB = 0.5, LB = –2000 Hz). TopSpin 2.1 (Bruker) program was used for spectra processing. The ZrO₂-rotor background was removed by subtracting the empty rotor spectrum.

$$\text{Carbon – based Selectivity}_{\text{EG}} = \frac{n(\text{EG})}{n(\text{EG}) + n(\text{EtOH}) + n(\text{MeCHO}) + n(\text{AcOH}) + 2n(\text{BuOH}) + n(\text{C2H6}) + n(1,1 - \text{Ethandiol}) + 0.5n(\text{CO2})} * 100\% \quad (5)$$

$$\text{Liquid – phase Selectivity}_{\text{EG}} = \frac{n(\text{EG})}{n(\text{EG}) + n(\text{EtOH}) + n(\text{MeCHO}) + n(\text{AcOH}) + n(\text{BuOH}) + n(1,1 - \text{Ethandiol})} * 100\% \quad (6)$$

$$\text{Carbon – based Selectivity}_{\text{PG}} = \frac{3n(\text{PG})}{3n(\text{PG}) + 3n(\text{lactic acid}) + 3n(\text{hydroxyacetone}) + n(\text{CO2})} * 100\% \quad (7)$$

$$\text{Liquid – phase Selectivity}_{\text{PG}} = \frac{n(\text{PG})}{n(\text{PG}) + n(\text{lactic acid}) + n(\text{hydroxyacetone})} * 100\% \quad (8)$$

Measurement of apparent quantum yield (AQY)

The reaction proceeded within the same batch reactor, using 200 mg catalyst dispersed in 50 mL DI H₂O, under 1 bar CO and 10 bar C₂H₄. The irradiation time is 60 min. The AQY of the photocatalytic system was determined according to Eq. 9, where NA, I, S and t represent Avogadro's constant, irradiation power density (mW/cm²), irradiation area (cm²) and irradiation time respectively. During this measurement, a 360 nm band pass filter was used to obtain monochromatic incident light. Therefore, the Eλ which stands for the energy of the incident photon can be calculated according to Eq. 10, where h and c represent Planck constant and light speed respectively. Note that due to the diversity of reaction pathways, the AQY in this study was calculated based only on the charges required to generate EG from C₂H₄ and H₂O, so it represents an underestimated value.

$$\text{AQY} = \frac{n(\text{reacted electrons})}{n(\text{incident photons})} * 100\% = \frac{n(\text{EG}) * 2 * NA}{ISt/E\lambda} * 100\% \quad (9)$$

$$E\lambda = hc/\lambda \quad (10)$$

DFT modeling

The computational work was performed with VASP 5.4 package^{58,59} in the periodic DFT framework. We used Perdew-Burke-Ernzerhof (PBE) functional⁶⁰, already known to be efficient for metallic surface calculation and also reported to be relevant for polyoxometalate (POM)^{23,61}. While POM structures were optimized in a 25x25x25 Å³ box at the Gamma point, metal slab computations were achieved with a 15 Å vacuum in the z direction to avoid interactions between virtual periodic images with a 2x2x1 k-mesh according to the Monkhorst-Pack scheme⁶². The projector augmented wave (PAW) method was used to describe the ion-electron interaction⁶³, with a cutoff-energy of 500 eV. In addition, a convergence criterion of 10⁻⁵ eV and of 0.05 eV/Å were adopted for electronic energy optimization and for ionic relaxation, respectively. All those parameters allow converging adsorption and reaction energy calculations with an accuracy of 0.05 eV. Note no zero-point energy (ZPE) and entropy correction were added.

With respect to the atomistic models, we considered a simplified POM model only including the Keggin (PW₁₂O₄₀³⁻) anion, the charge being delocalized all over the system. To simulate the anchored Pd clusters, we relaxed the POM structure with Pd₂ dimer embedded in

the surface into a quaternary site, denoted “Pd₂.NPW” in the following (Supplementary Fig. 26). Regarding Pd surface computations, we initially relaxed the *fcc* bulk structure reaching an optimal lattice parameter of 3.94 Å. Then we prepared a *p*(3×3) slab with a four atomic layer thickness, the two bottom layers being frozen in a bulk-like configuration. Reaction energy diagrams were established by taking ethylene and OH radical species in the gas phase as reference together with the bare catalyst surface (either Pd₂.NPW or Pd (111) slab). Note that OH radical energy is defined as the difference between H₂O and ½ H₂ energy in order to avoid uncertainty inherent to DFT calculations of radical species.

Data availability

All data presented in the main manuscript and Supplementary Information are provided as a source data file. Source data are provided with this paper.

References

1. Yue, H., Zhao, Y., Ma, X. & Gong, J. Ethylene glycol: properties, synthesis, and applications. *Chem. Soc. Rev.* **41**, 4218–4244 (2012).
2. Sullivan C. J., Kuenz A., Vorlop K.-D. Propanediols. In: *Ullmann's Encyclopedia of Industrial Chemistry* 1–29 (2018).
3. Gordon, C. P. et al. Efficient epoxidation over dinuclear sites in titanium silicalite-1. *Nature* **586**, 708–713 (2020).
4. Nijhuis, T. A., Makkee, M., Moulijn, J. A. & Weckhuysen, B. M. The production of propene oxide: catalytic processes and recent developments. *Ind. Eng. Chem. Res.* **45**, 3447–3459 (2006).
5. Schroeder, M. Osmium tetroxide cis hydroxylation of unsaturated substrates. *Chem. Rev.* **80**, 187–213 (1980).
6. Xie, S. et al. Visible light-driven C–H activation and C–C coupling of methanol into ethylene glycol. *Nat. Commun.* **9**, 1181 (2018).
7. Winiwarter, A. et al. Towards an atomistic understanding of electrocatalytic partial hydrocarbon oxidation: propene on palladium. *Energy Environ. Sci.* **12**, 1055–1067 (2019).
8. Lum, Y. et al. Tuning OH binding energy enables selective electrochemical oxidation of ethylene to ethylene glycol. *Nat. Catal.* **3**, 14–22 (2020).
9. Liu, X.-C. et al. Reaction mechanism and selectivity tuning of propene oxidation at the electrochemical interface. *J. Am. Chem. Soc.* **144**, 20895–20902 (2022).
10. Wang, L. et al. Precisely constructed metal sulfides with localized single-atom rhodium for photocatalytic c–h activation and direct methanol coupling to ethylene glycol. *Adv. Mater.* **35**, 2205782 (2022).
11. Fan, L. et al. Selective production of ethylene glycol at high rate via cascade catalysis. *Nat. Catal.* **6**, 585–595 (2023).
12. Ke, J. et al. Dynamically reversible interconversion of molecular catalysts for efficient electrooxidation of propylene into propylene glycol. *J. Am. Chem. Soc.* **145**, 9104–9111 (2023).
13. Xia, R. et al. Electrosynthesis of ethylene glycol from C1 feedstocks in a flow electrolyzer. *Nat. Commun.* **14**, 4570 (2023).
14. Zhang, S.-K. et al. Interfacial electrochemical-chemical reaction coupling for efficient olefin oxidation to glycols. *Joule* **7**, 1887–1901 (2023).
15. Li, A.-Z. et al. One-step electrochemical ethylene-to-ethylene glycol conversion over a multitasking molecular catalyst. *J. Am. Chem. Soc.* **146**, 5622–5633 (2024).
16. Cao, T. et al. Selective electrogenerative oxidation of 5-hydroxymethylfurfural to 2,5-furandialdehyde. *ChemSusChem* **10**, 4851–4854 (2017).
17. Shimura, K. & Yoshida, H. Hydrogen production from water and methane over Pt-loaded calcium titanate photocatalyst. *Energy Environ. Sci.* **3**, 615–617 (2010).
18. Dong, C. et al. Size-dependent activity and selectivity of carbon dioxide photocatalytic reduction over platinum nanoparticles. *Nat. Commun.* **9**, 1252 (2018).
19. Shoji, S. et al. Photocatalytic uphill conversion of natural gas beyond the limitation of thermal reaction systems. *Nat. Catal.* **3**, 148–153 (2020).
20. Qi, M.-Y., Conte, M., Anpo, M., Tang, Z.-R. & Xu, Y.-J. Cooperative coupling of oxidative organic synthesis and hydrogen production over semiconductor-based photocatalysts. *Chem. Rev.* **121**, 13051–13085 (2021).
21. Amthor, S. et al. A photosensitizer–polyoxometalate dyad that enables the decoupling of light and dark reactions for delayed on-demand solar hydrogen production. *Nat. Chem.* **14**, 321–327 (2022).
22. Dong, C. et al. Photocatalytic partial oxidation of methane to carbon monoxide and hydrogen over cigs solar cell. *Appl. Catal. B: Environ.* **325**, 122340 (2023).
23. Dong, C. et al. Direct photocatalytic synthesis of acetic acid from methane and co at ambient temperature using water as oxidant. *J. Am. Chem. Soc.* **145**, 1185–1193 (2023).
24. Zhou, P. et al. Solar-to-hydrogen efficiency of more than 9% in photocatalytic water splitting. *Nature* **613**, 66–70 (2023).
25. Zhang, Y. et al. H₂O₂ generation from O₂ and H₂O on a near-infrared absorbing porphyrin supramolecular photocatalyst. *Nat. Energy* **8**, 361–371 (2023).
26. He, C. et al. Constructing matched active sites for robust photocatalytic dry reforming of methane. *Chem* **9**, 3224–3244 (2023).
27. Li, Z. et al. Blocking the reverse reactions of overall water splitting on a Rh/GaN–ZnO photocatalyst modified with Al₂O₃. *Nat. Catal.* **6**, 80–88 (2023).
28. Habisreutinger, S. N., Schmidt-Mende, L. & Stolarczyk, J. K. Photocatalytic reduction of CO₂ on TiO₂ and other semiconductors. *Angew. Chem. Int. Ed. Engl.* **52**, 7372–7408 (2013).
29. Xu, L. et al. Highly selective photocatalytic synthesis of ethylene-derived commodity chemicals on BiOBr nanosheets. *Mater. Today Phys.* **21**, 100551 (2021).
30. Zhang, H. et al. C–H activations of methanol and ethanol and C–C couplings into diols by zinc–indium–sulfide under visible light. *Chem. Commun.* **56**, 1776–1779 (2020).
31. Ma, J. et al. Efficient photoelectrochemical conversion of methane into ethylene glycol by WO₃ nanobar arrays. *Angew. Chem. Int. Ed. Engl.* **60**, 9357–9361 (2021).
32. Yu, X. et al. Stoichiometric methane conversion to ethane using photochemical looping at ambient temperature. *Nat. Energy* **5**, 511–519 (2020).
33. Khivantsev, K. et al. Stabilization of super electrophilic Pd²⁺ cations in small-Pore SSZ-13 zeolite. *J. Phys. Chem. C* **124**, 309–321 (2020).
34. Dong, C. et al. Fully exposed palladium cluster catalysts enable hydrogen production from nitrogen heterocycles. *Nat. Catal.* **5**, 485–493 (2022).
35. Wang, Y. et al. In-situ exploration of divergent methane coupling pathways in dry and aqueous environments on silver and palladium heteropolyacid-titania photocatalysts. *Appl. Catal. B: Environ. Energy* **358**, 124400 (2024).
36. Chen, G., Li, R. & Huang, L. Advances in photochemical deposition for controllable synthesis of heterogeneous catalysts. *Nanoscale* **15**, 13909–13931 (2023).
37. Tran, M. N. et al. Boosting gas-phase TiO₂ photocatalysis with weak electric field strengths of volt/centimeter. *ACS Appl. Mater. Interfaces* **16**, 14852–14863 (2024).
38. Wang, W. et al. In situ protonated-phosphorus interstitial doping induces long-lived shallow charge trapping in porous C_{3-x}N₄ photocatalysts for highly efficient H₂ generation. *Energy Environ. Sci.* **16**, 460–472 (2023).
39. Kolb, H. C., VanNieuwenhze, M. S. & Sharpless, K. B. Catalytic asymmetric dihydroxylation. *Chem. Rev.* **94**, 2483–2547 (1994).
40. Filowitz, M., Ho, R. K. C., Klemperer, W. G. & Shum, W. Oxygen-17 nuclear magnetic resonance spectroscopy of polyoxometalates. 1. Sensitivity and resolution. *Inorg. Chem.* **18**, 93–103 (1979).

41. Bastow, T. J., Moodie, A. F., Smith, M. E. & Whitfield, H. J. Characterisation of titania gels by ^{17}O nuclear magnetic resonance and electron diffraction. *J. Mater. Chem.* **3**, 697–702 (1993).
42. Xiang, Q., Yu, J. & Wong, P. K. Quantitative characterization of hydroxyl radicals produced by various photocatalysts. *J. Colloid Interface Sci.* **357**, 163–167 (2011).
43. Shimoaka, T. & Hasegawa, T. Molecular structural analysis of hydrated ethylene glycol accounting for the antifreeze effect by using infrared attenuated total reflection spectroscopy. *J. Mol. Liq.* **223**, 621–627 (2016).
44. Bodoardo, S., Chiappetta, R., Onida, B., Figueras, F. & Garrone, E. Ammonia interaction and reaction with Al-pillared montmorillonite: an IR study. *Microporous Mesoporous Mater.* **20**, 187–196 (1998).
45. Hawkins, M. & Andrews, L. Reactions of atomic oxygen with ethene in solid argon. The infrared spectrum of vinyl alcohol. *J. Am. Chem. Soc.* **105**, 2523–2530 (1983).
46. Hill, J. M., Shen, J., Watwe, R. M. & Dumesic, J. A. Microcalorimetric, infrared spectroscopic, and dft studies of ethylene adsorption on pd and pd/sn catalysts. *Langmuir* **16**, 2213–2219 (2000).
47. Resasco, J. et al. Relationship between atomic scale structure and reactivity of pt catalysts: hydrodeoxygenation of m-cresol over isolated pt cations and clusters. *ACS Catal.* **10**, 595–603 (2019).
48. Ravel, B. & Newville, M. ATHENA, ARTEMIS, HEPHAESTUS: data analysis for X-ray absorption spectroscopy using IFEFFIT. *J. Synchrotron Radiat.* **12**, 537–541 (2005).
49. Newville, M. EXAFS analysis using FEFF and FEFFIT. *J. Synchrotron Radiat.* **8**, 96–100 (2001).
50. Rehr, J. J. & Albers, R. C. Theoretical approaches to x-ray absorption fine structure. *Rev. Mod. Phys.* **72**, 621–654 (2000).
51. Escobar-Bedia, F. J. et al. Active and regioselective Ru single-site heterogeneous catalysts for alpha-olefin hydroformylation. *ACS Catal.* **12**, 4182–4193 (2022).
52. Newville M. Larch: An analysis package for XAFS and related spectroscopies. *J. Phys.: Conference Series* **430**, 1–7 (2013).
53. Gao, T. et al. Covalent organic framework derived synthesis of Ru embedded in carbon nitride for hydrogen and oxygen evolution reactions. *J. Mater. Chem. A* **11**, 19338–19348 (2023).
54. Wang, W. et al. Near-field drives long-lived shallow trapping of polymeric c₃n₄ for efficient photocatalytic hydrogen evolution. *Adv. Funct. Mater.* **31**, 2103978 (2021).
55. Liu, L.-J. et al. NIR-II emissive anionic copper nanoclusters with intrinsic photoredox activity in single-electron transfer. *Nat. Commun.* **15**, 4688 (2024).
56. Ai, S., Wang, Q., Li, H. & Jin, L. Study on production of free hydroxyl radical and its reaction with salicylic acid at lead dioxide electrode. *J. Electroanalytical Chem.* **578**, 223–229 (2005).
57. Wang, K., Li, Y., Zhang, G., Li, J. & Wu, X. OD Bi nanodots/2D Bi₃NbO₇ nanosheets heterojunctions for efficient visible light photocatalytic degradation of antibiotics: Enhanced molecular oxygen activation and mechanism insight. *Appl. Catal. B: Environ.* **240**, 39–49 (2019).
58. Kresse, G. & Hafner, J. Ab initio molecular dynamics for open-shell transition metals. *Phys. Rev. B* **48**, 13115–13118 (1993).
59. Kresse, G. & Furthmüller, J. Efficient iterative schemes for ab initio total-energy calculations using a plane-wave basis set. *Phys. Rev. B* **54**, 11169–11186 (1996).
60. Perdew, J. P., Burke, K. & Ernzerhof, M. Generalized gradient approximation made simple. *Phys. Rev. Lett.* **77**, 3865–3868 (1996).
61. Zhang, L. et al. Catalytic selective oxidation of isobutane in a decoupled redox-process. *Appl. Catal. A: Gen.* **643**, 118798 (2022).
62. Monkhorst, H. J. & Pack, J. D. Special points for Brillouin-zone integrations. *Phys. Rev. B* **13**, 5188–5192 (1976).
63. Kresse, G. & Joubert, D. From ultrasoft pseudopotentials to the projector augmented-wave method. *ultrasoft pseudopotentials projector augmented-wave method* **59**, 1758–1775 (1999).

Acknowledgements

This research is being performed within the ANR SolarMethaChem project (ANR-20-SODR-0002) and PEPR Spleen ECOCHEM. The authors gratefully acknowledge the support of the French National Research Agency (ANR). Y. W. thanks the China Scholarship Council for PhD stipend. The Swiss Light Source and SuperXAS beam line is acknowledged for the use of synchrotron beam and in-situ experimental setup.

Author contributions

C.D., V.V.O., and A.Y.K. conceived the idea for this work. All authors contributed to the design of the experimental setup and experimental procedures. C.D. and Y.W. prepared the catalysts, and performed photocatalytic tests. C.D., J.-C.M, M.D., M.T., Y.K., and Y.W. performed in-situ or ex-situ catalyst characterization using FT-IR, STEM, XPS, and NMR. M.M. performed STEM-HAADF and EDS measurements. K.B.T. characterized the catalyst and reaction intermediate using EPR. C.D., V.V.O, O.S., and A.Y.K. carried out in-situ XAS measurements and analysis. V.M.D. performed the XAS results fitting and analysis. M.N.T. performed the photoluminescence measurement. Z.D., W.W., and C.D. performed femtosecond transient absorption spectroscopy and results analysis. J.Z. performed DFT modeling. C.D., A.Y.K., and V.V.O. wrote the draft and all authors took part in improving the manuscript.

Competing interests

The authors declare no competing interests.

Additional information

Supplementary information The online version contains supplementary material available at <https://doi.org/10.1038/s41467-024-52461-9>.

Correspondence and requests for materials should be addressed to Andrei Y. Khodakov or Vitaly V. Ordonsky.

Peer review information *Nature Communications* thanks Jingyu Wang and the other, anonymous, reviewers for their contribution to the peer review of this work. A peer review file is available.

Reprints and permissions information is available at <http://www.nature.com/reprints>

Publisher's note Springer Nature remains neutral with regard to jurisdictional claims in published maps and institutional affiliations.

Open Access This article is licensed under a Creative Commons Attribution-NonCommercial-NoDerivatives 4.0 International License, which permits any non-commercial use, sharing, distribution and reproduction in any medium or format, as long as you give appropriate credit to the original author(s) and the source, provide a link to the Creative Commons licence, and indicate if you modified the licensed material. You do not have permission under this licence to share adapted material derived from this article or parts of it. The images or other third party material in this article are included in the article's Creative Commons licence, unless indicated otherwise in a credit line to the material. If material is not included in the article's Creative Commons licence and your intended use is not permitted by statutory regulation or exceeds the permitted use, you will need to obtain permission directly from the copyright holder. To view a copy of this licence, visit <http://creativecommons.org/licenses/by-nc-nd/4.0/>.

© The Author(s) 2024